

Intraband Spin-Dependent Recombination of Bound Holes in Silicon

Daejin Eom¹* and Ja-Yong Koo

Korea Research Institute of Standards and Science, Yuseong, Daejeon 34113, Republic of Korea



(Received 15 June 2021; accepted 24 November 2021; published 15 December 2021)

We generate paramagnetic centers on a heavily boron-doped Si(111) surface by using a scanning tunneling microscope and show that they mediate the spin-dependent recombination of the bound holes of the boron acceptor via direct visualization. This recombination is the intraband process and is significantly affected by the spin-orbit coupling effect. We also demonstrate that such a paramagnetic center with a boron acceptor at its neighbor site can be produced with atomic precision, which makes it a promising candidate for implementing position-controlled impurity qubits with an electrical readout mechanism in silicon.

DOI: 10.1103/PhysRevLett.127.256801

Recombination is a major depletion process of excess charge carriers in semiconductors that limits the performance of electronic and optoelectronic devices significantly [1–3]. Recently, spin-dependent recombination finds new applications in the field of solid-state quantum technologies by providing an electrical readout mechanism of the quantum information stored in the nuclear spin [4,5]. This spin-dependent process is often explained by the Kaplan-Solomon-Mott (KSM) model, where both a shallow trap and a paramagnetic center are generated in close spatial proximity to each other with distinct energy states in the band gap [6–8]. A free electron is then captured by the trap to form a spin pair with the electron in the paramagnetic center. If they are in the singlet (triplet) state, the electron in the trap can (cannot) hop into the paramagnetic center to combine with a hole in the valence band. The experimental observation of such a phenomenon goes back to as early as the optical work by Geschwind, Collins, and Schawlow in 1959 [9] and the electrical one by Lepine in 1972 [10]. However, space-averaging measurements like photoconductivity [10,11] or ESR spectroscopy [12] have failed to unravel the geometric and orbital structures of the spin-dependent recombination centers via direct visualization.

Here, we employ a scanning tunneling microscope (STM) to generate paramagnetic structures on a heavily boron-doped Si(111) surface and show that they work as spin-dependent recombination centers with two distinct features. First, the paramagnetic state is located below the valence band maximum (VBM), not in the band gap, which leads to the spin-dependent recombination of the injected hole with the electron in the valence band. This intraband recombination contrasts to the KSM model, where the hole in the valence band recombines with the electron in the conduction band at the paramagnetic state in the band gap [6,7]. To our best knowledge, it is the first of this kind of spin-dependent recombination process. Second, the paramagnetic center has a boron acceptor at its nearest-neighbor site, suggesting that this

composite system may possibly be exploited as an electrically readable impurity qubit [13–15]. Also, we demonstrate that such a composite system can be produced with atomic precision on the Si surface. Hence, it may resolve two technical obstacles to the scale-up of impurity-based quantum devices, i.e., atomistic control of the impurity position and incorporation of an electrical readout mechanism.

Our experiments were carried out using low-temperature STM in an ultrahigh-vacuum chamber, whose base pressure was below 1×10^{-10} Torr. Heavily boron-doped crystalline Si with the (111) orientation and a resistivity of $< 0.01 \Omega\text{cm}$ was cleaned *in situ* by repeated thermal flashes at ~ 1370 K. It was then cooled down to room temperature at a rate of ~ 2 K/s after the last flash. After that, it was quenched down to ~ 4.5 K for the STM measurements. The magnetic field (B) was applied normal to the Si surface up to 7 T. The STM probe tip was made of Pt-Ir alloy.

Figure 1(a) shows the STM topography of a heavily boron-doped Si(111) surface with the $\sqrt{3} \times \sqrt{3}$ reconstruction whose lattice parameter is 0.67 nm [16]. Its structural model is displayed in Fig. 1(c), where the boron atom occupies one-third of the third-layer sites (S_5 site) and the topmost Si adatom is sitting directly above the boron atom (T_4 site) [17,18]. We then apply high-bias pulses between a probe tip and the substrate with the feedback loop off to generate the adatom vacancy on the Si(111) surface [19]. Its topography is displayed in Fig. 1(b) along with its structural model in Fig. 1(d). We will term this adatom vacancy with the underlying boron atom as the BV complex hereafter, meaning the boron-vacancy complex. This BV complex evolves three spectral features (Ψ_2 , Ψ_3 , and Ψ_4) within the band gap and another one (Ψ_1) below the VBM [see Fig. 1(e)]. As addressed in Ref. [19], they have the spectral origin from three Si dangling bonds (DBs) of the BV complex: The electronic interactions of three DBs produce a doubly degenerate level (E_e) near the VBM and a nondegenerate one (E_a) near the conduction band minimum [see Fig. 1(f)]. However, the E_e

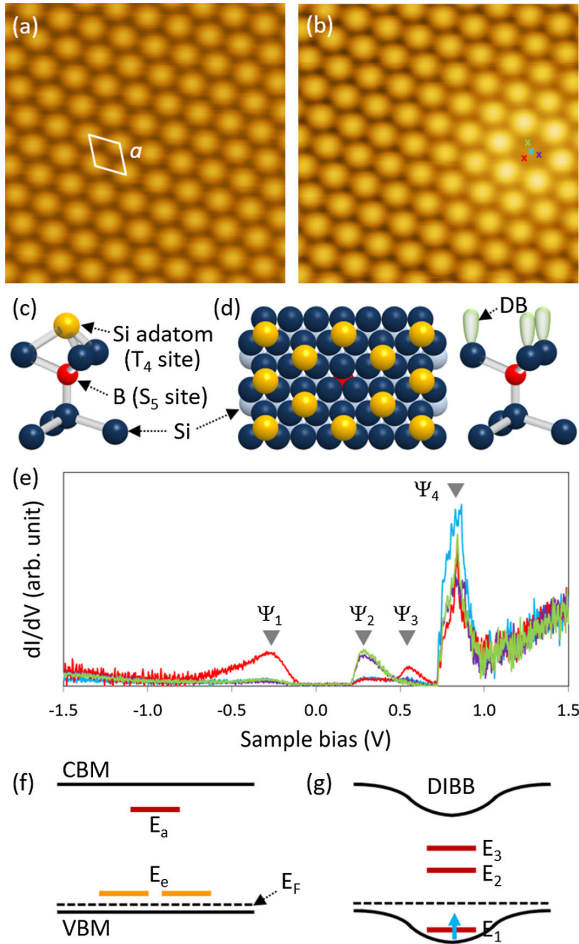


FIG. 1. (a) Topography of a heavily boron-doped Si(111) surface, whose lateral dimension is $6.2 \times 6.2 \text{ nm}^2$. It is probed with a sample bias (V_{sample}) of 2.5 V and a tunneling current (I_t) of 0.5 nA. $a = 0.67 \text{ nm}$. (b) Topography of the same area as that in (a) but taken after a Si adatom is removed by the application of a high-bias pulse [19]. It is probed with $V_{\text{sample}} = 2.5 \text{ V}$ and $I_t = 0.5 \text{ nA}$. (c),(d) Structural models of (c) the intact surface and (d) the BV complex. The top view with a missing adatom is also presented in (d). (e) Tunneling conductance (dI/dV) spectra probed at four different positions within the BV complex as marked by the crosses in (b). They are displayed with the same colors as the corresponding crosses. Ψ_1 , Ψ_2 , Ψ_3 , and Ψ_4 indicate four distinct spectral features of the BV complex. (f),(g) Energy diagrams of the BV complex (f) before and (g) after the Jahn-Teller transition. The DIBB effect is superimposed in (g).

level accommodates only one electron in it (see the analysis in Ref. [19]), which drives the BV complex to undergo the Jahn-Teller transition and lifts E_e into separate levels, one below and the other above the Fermi level (E_F) [see Fig. 1(g)]. The Ψ_1 , Ψ_2 , and Ψ_3 features in Fig. 1(e) correspond to the E_1 , E_2 , and E_3 levels in Fig. 1(g), respectively. The Ψ_4 feature in Fig. 1(e), on the other hand, results from the additional release of electron from the BV complex due to the tip-induced band bending (TIBB) at $V_{\text{sample}} \gtrsim 0.52 \text{ V}$ and corresponds to the E_a level in Fig. 1(f) (see the analysis in Ref. [19]).

Of particular interest is that the BV complex exhibits field-dependent tunneling behavior, although the intact surface does not. Figures 2(b) and 2(c) are the tunneling current spectra measured at the Si adatom (not shown) and at the center of the BV complex in Fig. 2(a), respectively, with the magnetic field applied perpendicular to the sample surface. The former does not show any appreciable field dependence as expected for the Si material. On the other hand, the tunneling spectra of the BV complex vary significantly with the field strength, especially in the valence band region. It implies that the electron tunneling from the BV complex to the tip is a field-dependent or spin-dependent process. Also, such field dependence is not monotonic but has a peak structure as Fig. 2(d) displays. This behavior is a consequence of rather a complex mechanism which we will elaborate in the later part of this paper.

The field dependence of the tunneling current is most prominent near the center of the BV complex and gets very weak at its periphery. To visualize this spatial variation of the field dependence, we have measured the difference spectrum between two current spectra taken at two different field strengths, say, 1 and 7 T, and then plotted its constant-bias map. Figure 3(f) is a typical example of the difference spectrum map taken in the same area as the topography of

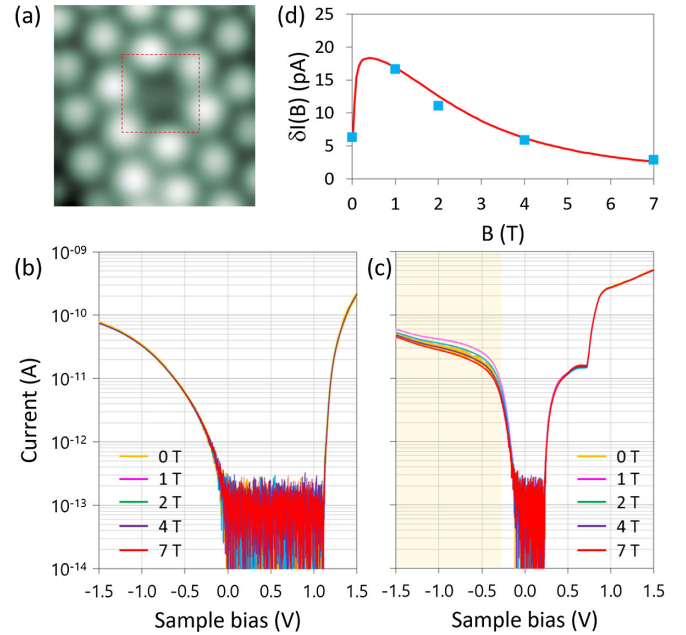


FIG. 2. (a) Topography of the BV complex, which is probed with $V_{\text{sample}} = 2.5 \text{ V}$ and $I_t = 1.0 \text{ nA}$ and has the lateral dimension of $3 \times 3 \text{ nm}^2$. (b),(c) Variations of the tunneling current spectra with the magnetic field strength. They are taken (b) on top of the adatom and (c) at the center of the BV complex in (a). (d) Field-dependent change of the tunneling current values at $V_{\text{sample}} = -0.7 \text{ V}$. The red curve is the fit to the measured data (square symbols) by Eq. (7) with $\alpha = 0.15$, $\gamma = 0.00015$, $t = 4.6 \times 10^{-5} \text{ eV}$, and $\Gamma_{\text{rel}} = 29 \text{ MHz}$.

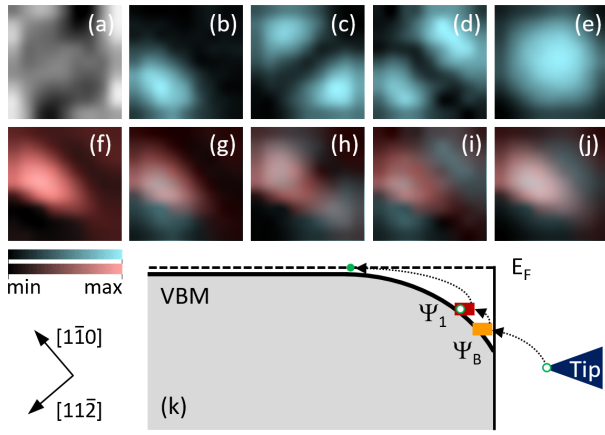


FIG. 3. (a) Topography of the BV complex whose region is marked by the dashed line in Fig. 2(a). It has the lateral dimension of $0.9 \times 0.9 \text{ nm}^2$ and is probed with $V_{\text{sample}} = 2.0 \text{ V}$ and $I_t = 1.0 \text{ nA}$. (b)–(e) Squared wave functions of Ψ_1 , Ψ_2 , Ψ_3 , and Ψ_4 , respectively, which are taken in the same area as that in (a). Their scale bar shown in blue in the left bottom ranges from 0 to 295 pA/V, from 10 to 314 pA/V, from 0 to 196 pA/V, and from 118 to 1784 pA/V for (b), (c), (d), and (e), respectively. (f) Map of the difference spectrum, $I(V; B = 1 \text{ T}) - I(V; B = 7 \text{ T})$, taken in the same area as that in (a) with $V_{\text{sample}} = -0.7 \text{ V}$. Its scale bar shown in red in the left bottom ranges from -5 to 22 pA . (g)–(j) The same images as those in (b)–(e), respectively, but overlaid by the map in (f). (k) Schematic of the energy diagram of Ψ_1 and Ψ_B states. Ψ_1 holds a hole (open circle) in it to be a paramagnetic center. Another hole is injected from the STM tip to Ψ_B and then hops to Ψ_1 to recombine with an electron (closed circle) at E_F .

the BV complex in Fig. 3(a). It shows that the difference spectrum is strong near the center of the BV complex and gets weaker at the off-center positions. Noteworthy is that this field-dependent region (Ψ_B) is different from the spatial extents of Ψ_1 , Ψ_2 , Ψ_3 , and Ψ_4 states in Fig. 1(e). The latter is displayed in Figs. 3(b)–3(e), respectively, and is overlaid by Ψ_B in Figs. 3(g)–3(j) for direct comparison. Figure 3(g), for example, shows that the center of the spectral weight of Ψ_B is located near the center of the BV complex along the $[11\bar{2}]$ direction, whereas that of the Ψ_1 state is located at the off-center position. This observation indicates that Ψ_B is a separate orbital state other than Ψ_1 , Ψ_2 , Ψ_3 , and Ψ_4 . Since the boron acceptor is located near the center of the BV complex even after the Jahn-Teller distortion, we ascribe the nature of Ψ_B to an acceptor-related one like the bound-hole state: The anisotropic or squeezed shape of Ψ_B in Fig. 3(f) is likely caused by the local strain that is either present naturally with the vacancy structure or induced by the Jahn-Teller distortion. In fact, a bound hole has different effective masses (m_{eff}) along and perpendicular to the strain direction [20], which leads to the anisotropy of the effective Bohr radius (r_B) via the mutual antiproportionality, i.e., $r_B \sim m_{\text{eff}}^{-1}$ [21]. The spatial extent of Ψ_B in Fig. 3(f) is rather small ($\sim 0.34 \text{ nm}$ along the $[1\bar{1}0]$ direction and $\sim 0.17 \text{ nm}$ along the $[11\bar{2}]$ direction) when compared to the effective

Bohr radius of a bound-hole state within bulk Si ($\sim 1.3 \text{ nm}$) [22]. However, the boron acceptor in question is nearly exposed to the vacuum as illustrated in Fig. 1(d). Thus, the dielectric screening (ϵ_{eff}) within the BV complex would be much weaker than deep in the bulk, letting the bound-hole state have a reduced Bohr radius ($r_B \sim \epsilon_{\text{eff}}$).

The field dependence of the current spectra in Fig. 2(c) becomes prominent at $\lesssim -0.3 \text{ eV}$, i.e., below the energy level of the Ψ_1 state. It suggests that Ψ_1 is also involved in the field-dependent tunneling process observed in the Ψ_B region. The former may constitute a major conduction path to and from the latter, with the charge transfer between them being affected by the magnetic fields due to the unpaired electron in Ψ_1 . To elaborate this mechanism further, we regard the paramagnetic state Ψ_1 as holding one hole in the two-electron background. The Ψ_B state, on the other hand, has bound-hole character and, thus, holds zero hole in it in the stationary state, because its energy level is located below E_F due to the defect-induced band bending (DIBB) (see the analysis in Ref. [19]). Once a hole is injected into the Ψ_B state from the STM tip, it will hop to the Ψ_1 state to combine with an electron at E_F or the VBM [see Fig. 3(k)]. This charge transfer process can be described as $(1, 0) \rightarrow (1, 1) \rightarrow (2, 0) \rightarrow (1, 0)$, where (n, m) denotes the hole configuration in Ψ_1 and Ψ_B , respectively. Since the $(2, 0)$ configuration has a spin singlet due to the Pauli exclusion principle, the hole transfer from Ψ_B to Ψ_1 in the $(1, 1)$ configuration will depend on the relative spin orientations of the two holes. Especially, the hole transfer in the triplet $(1, 1)$ configuration would be blocked unless it mixes with the singlet one by the spin relaxation process. This relaxation may be driven by the hyperfine interaction with the nuclear spin [23, 24] or the spin-orbit interaction with orbital, Rashba, and/or Dresselhaus effects [25–28]. Indeed, previous studies [23–28] show that those interactions lift the spin blockade to yield a field-dependent peak structure in the leakage current, as does the tunneling current in Fig. 2(d). The width of the current peak due to the hyperfine interaction, however, is comparable to the magnitude of the effective nuclear field [23, 24], which we estimate to be less than 10 mT for the boron acceptor [29]. Since the tunneling current in Fig. 2(d) has a peak width on the scale of $\sim 1 \text{ T}$, we ascribe its origin to the spin-orbit coupling rather than the hyperfine interaction as addressed in detail below.

We consider a model Hamiltonian for the spin-orbit coupling effect on the leakage current of double quantum dots [25]:

$$H = H_m + H_e + H_t \quad (1)$$

with

$$H_m = g\mu_B B S_z^{\text{tot}}, \quad (2)$$

$$H_e = \Delta |S_{20}\rangle \langle S_{20}|, \quad (3)$$

$$H_t = \sum_{s,s' \in \{\uparrow\downarrow\}} (t_1^{ss'} c_{1s}^\dagger c_{2s'} + t_2^{ss'} c_{2s}^\dagger c_{1s'}), \quad (4)$$

where H_m is the Zeeman energy of two holes due to the applied magnetic field B . S^{tot} is the total spin of two holes, and g is the g factor. H_e (H_t) describes the electronic detuning (kinetic hopping energy) between Ψ_1 and Ψ_B . The bra and ket symbols are introduced such that $|S_{20}\rangle$ and $|S\rangle$ represent the singlet states of (2,0) and (1,1) configurations, respectively. Also, $|T_+\rangle$, $|T_-\rangle$, and $|T_0\rangle$ are the triplet states of the (1,1) configuration with $m = +1, -1$, and 0 , respectively. If we introduce orthogonal unpolarized triplet states $|T_{x,y}\rangle = i^{(1/2) \mp (1/2)} (|T_-\rangle \mp |T_+\rangle) / \sqrt{2}$ and $|T_z\rangle = |T_0\rangle$, then H_t can be written as [25,26]

$$H_t = i\vec{t} \cdot \vec{|T\rangle} \langle S_{20}| + t|S\rangle \langle S_{20}| + \text{H.c.}, \quad (5)$$

where $\vec{t} = (t_x, t_y, t_z)$ and $\vec{|T\rangle} = (|T_x\rangle, |T_y\rangle, |T_z\rangle)$ with t (\vec{t}) being the spin-conserving (non-spin-conserving) hopping energy (energies). Now we evaluate the charge dynamics or leakage current governed by the model Hamiltonian in Eq. (1) by using the density matrix approach [30,31]. If ρ is the hole density matrix, then its time evolution is determined by [25,26]

$$\frac{d\rho}{dt} = \frac{1}{i\hbar} [H, \rho] + \Gamma\rho + \Gamma_{\text{rel}}\rho, \quad (6)$$

where the operator Γ describes the decay of $|S_{20}\rangle$ to the (1,0) configuration and the subsequent hole capture into the (1,1) configuration. The operator Γ_{rel} describes the transition between four (1,1) states due to the spin mixing or relaxation processes. We assume that Γ_{rel} has much smaller magnitude than Γ . Also, we simplify our analysis by assuming that t_x , t_y , and t_z in Eq. (5) have the same magnitude (say, t_{so}), that the spin relaxation of each (1,1) state to another (1,1) state by Γ_{rel} is identical, and that the detuning Δ in Eq. (3) is zero. Then, Eq. (6) can be solved in the stationary condition $d\rho/dt = 0$ to yield the field-dependent leakage current as follows [25]:

$$\delta I(B) = e\Gamma_{\text{rel}} \frac{[\chi - (g\mu_B B)^2 + \tau^2][\chi(1 + 4\gamma) + (g\mu_B B)^2 - \tau^2]}{6\gamma\chi^2 + 2\alpha^2 t^2 (g\mu_B B)^2}, \quad (7)$$

where $\alpha = t_{so}/t$, $\gamma = \Gamma_{\text{rel}}/\Gamma$, $\tau = t\sqrt{1 + 3\alpha^2}$, and $\chi = \sqrt{[(g\mu_B B)^2 - \tau^2]^2 + 8\alpha^2 t^2 (g\mu_B B)^2}$.

The red curve in Fig. 2(d) is a fit to the experimental data by Eq. (7) with $\alpha = 0.15$, $\gamma = 0.00015$, $t = 4.6 \times 10^{-5}$ eV, and $\Gamma_{\text{rel}} = 29$ MHz, which reproduces the peak structure with good fitting quality [32]. The α value of 0.15 is comparable to the reported one (i.e., $\alpha \sim 0.13$) for hole

transfer via double quantum dots formed on a p -type silicon surface [33]. These values indicate that the effective spin-orbit interaction causing non-spin-conserving transition between the (1,1) triplet and (2,0) singlet is quite significant though not in the strong limit. The Γ_{rel} value determines the time span of the rate-limiting relaxation process as $\Gamma_{\text{rel}}^{-1} = (29 \text{ MHz})^{-1} = 35 \text{ ns}$ [32], which is very close to the lifetime of minority carriers in heavily ($n \sim 10^{19} \text{ cm}^{-3}$) boron-doped Si like our sample [34]. On the other hand, the hopping energy t between Ψ_1 and Ψ_B is much smaller than those between Si DBs [35,36]. Several factors including the electron-phonon interaction and different orbital natures of Ψ_1 and Ψ_B can be responsible for the small t value. For example, Ψ_1 is the Jahn-Teller distorted state holding one carrier in it [19], and, thus, the charge transfer process between Ψ_1 and Ψ_B should be accompanied by the excitation of many Jahn-Teller phonons, which will renormalize the hopping energy by the electron-phonon coupling constant (λ) as $t \sim t_0 e^{-\lambda^2}$ [37,38]. Since a typical λ^2 value in the surface region of our sample is ~ 8 [16], the effective hopping energy will be reduced by the multiplication factor of $e^{-\lambda^2} \sim 3.4 \times 10^{-4}$. It explains the small value of the observed t parameter to a large extent.

As Kane has proposed [39], the nuclear spin of an impurity atom near the Si surface is an excellent candidate for the quantum memory. The majority of boron isotopes in nature have a nuclear spin of $3/2$ [15], and, thus, the boron acceptor in the BV complex may possibly be exploited as a spin-3/2 qubit [13,14]. Also, the spin-dependent recombination of the injected holes in the BV complex provides an electrical readout mechanism for the nuclear spin state of the boron acceptor [4], though the magnetoresistive technique using an ESR STM with a magnetic tip can be an alternative, which has been used to probe the hyperfine splitting in certain isotopes [40]. In addition, the BV complex can be

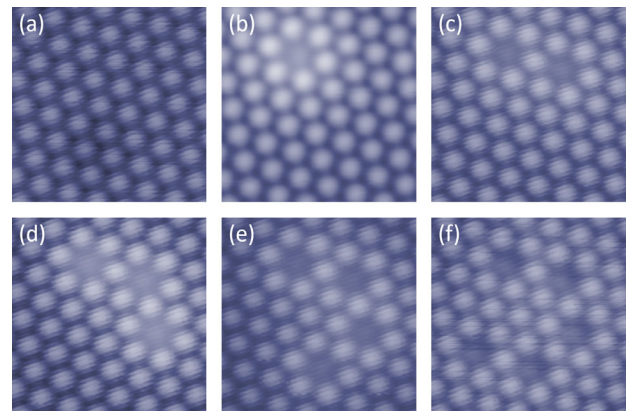


FIG. 4. (a)–(f) A series of STM topographies taken sequentially over the same area. They have a lateral dimension of $4.7 \times 4.7 \text{ nm}^2$ and are probed with $V_{\text{sample}} = 2.5 \text{ V}$ and $I_t = 0.3 \text{ nA}$. Before taking each image, a high-bias pulse is applied to generate a new BV complex [19].

generated on the Si(111) surface with atomic precision by using an STM tip as demonstrated in Fig. 4. Hence, the BV complex may resolve two technical obstacles to the scale-up of impurity-based quantum devices, i.e., atomistic control of the impurity position and incorporation of an electrical readout mechanism.

This work was supported by Korea Research Institute of Standards and Science (KRISS-GP2021-0009-08).

*d.eom@kriss.re.kr

- [1] W. Shockley and W. T. Read, Jr., *Phys. Rev.* **87**, 835 (1952).
- [2] R. N. Hall, *Phys. Rev.* **87**, 387 (1952).
- [3] F. C. Rong, W. R. Buchwald, E. H. Poindexter, W. L. Warren, and D. J. Keeble, *Solid-State Electron.* **34**, 835 (1991).
- [4] A. R. Stegner, C. Boehme, H. Huebl, M. Stutzmann, K. Lips, and M. S. Brandt, *Nat. Phys.* **2**, 835 (2006).
- [5] L. Dreher, F. Hoehne, M. Stutzmann, and M. S. Brandt, *Phys. Rev. Lett.* **108**, 027602 (2012).
- [6] D. Kaplan, I. Solomon, and N. F. Mott, *J. Phys. Lett.* **39**, 51 (1978).
- [7] C. Boehme and K. Lips, *Phys. Rev. B* **68**, 245105 (2003).
- [8] C. Boehme and K. Lips, *Phys. Rev. Lett.* **91**, 246603 (2003).
- [9] S. Geschwind, R. J. Collins, and A. L. Schawlow, *Phys. Rev. Lett.* **3**, 545 (1959).
- [10] D. J. Lepine, *Phys. Rev. B* **6**, 436 (1972).
- [11] F. Zhao, A. Balocchi, A. Kunold, J. Carrey, H. Carrère, T. Amand, N. B. Abdallah, J. C. Harmand, and X. Marie, *Appl. Phys. Lett.* **95**, 241104 (2009).
- [12] L. S. Vlasenko, Y. V. Martynov, T. Gregorkiewicz, and C. A. J. Ammerlaan, *Phys. Rev. B* **52**, 1144 (1995).
- [13] A. R. Kessel and V. L. Ermakov, *J. Exp. Theor. Phys. Lett.* **70**, 61 (1999).
- [14] G. B. Furman, V. M. Meerovich, and V. L. Sokolovsky, *Hyperfine Interact.* **198**, 153 (2010).
- [15] C. Kittel, *Introduction to Solid State Physics*, 6th ed. (Wiley, Singapore, 1991).
- [16] D. Eom, C.-Y. Moon, and J.-Y. Koo, *Nano Lett.* **15**, 398 (2015).
- [17] I.-W. Lyo, E. Kaxiras, and Ph. Avouris, *Phys. Rev. Lett.* **63**, 1261 (1989).
- [18] R. L. Headrick, I. K. Robinson, E. Vlieg, and L. C. Feldman, *Phys. Rev. Lett.* **63**, 1253 (1989).
- [19] D. Eom, C.-Y. Moon, and J.-Y. Koo, *Phys. Rev. B* **100**, 115302 (2019).
- [20] T. Guillaume and M. Mouis, *Solid-State Electron.* **50**, 701 (2006).
- [21] M. J. Schmidt, K. Pappert, C. Gould, G. Schmidt, R. Oppermann, and L. W. Molenkamp, *Phys. Rev. B* **76**, 035204 (2007).
- [22] M. Lax and E. Burstein, *Phys. Rev.* **100**, 592 (1955).
- [23] O. N. Jouravlev and Y. V. Nazarov, *Phys. Rev. Lett.* **96**, 176804 (2006).
- [24] J. Danon, X. Wang, and A. Manchon, *Phys. Rev. Lett.* **111**, 066802 (2013).
- [25] A. Zarassi, Z. Su, J. Danon, J. Schwenderling, M. Hocevar, B. M. Nguyen, J. Yoo, S. A. Dayeh, and S. M. Frolov, *Phys. Rev. B* **95**, 155416 (2017).
- [26] J. Danon and Y. V. Nazarov, *Phys. Rev. B* **80**, 041301(R) (2009).
- [27] P. Harvey-Collard, N. T. Jacobson, C. Bureau-Oxton, R. M. Jock, V. Srinivasa, A. M. Mounce, D. R. Ward, J. M. Anderson, R. P. Manginell, J. R. Wendt, T. Pluym, M. P. Lilly, D. R. Luhman, M. Pioro-Ladrière, and M. S. Carroll, *Phys. Rev. Lett.* **122**, 217702 (2019).
- [28] I. Gierz, T. Suzuki, E. Frantzeskakis, S. Pons, S. Ostanin, A. Ernst, J. Henk, M. Grioni, K. Kern, and C. R. Ast, *Phys. Rev. Lett.* **103**, 046803 (2009).
- [29] M. Sprenger, R. van Kemp, E. G. Sieverts, and C. A. J. Ammerlaan, *Phys. Rev. B* **35**, 1582 (1987).
- [30] J. J. Sakurai, *Modern Quantum Mechanics*, 1st ed. (Addison-Wesley, Redwood City, CA, 1985).
- [31] K. Huang, *Statistical Mechanics*, 2nd ed. (Wiley, Singapore, 1987).
- [32] The parameter ranges of Eq. (7) for the acceptable fitting quality in Fig. 2(d) are $\alpha = 0.15 \pm 0.02$, $\gamma = (1.5 \pm 0.5) \times 10^{-4}$, $t = (4.6 \pm 0.6) \times 10^{-5}$ eV, and $\Gamma_{\text{rel}} = 29 \pm 10$ MHz. From the last parameter range, we deduce that $\Gamma_{\text{rel}}^{-1} = 35 \pm 9$ ns.
- [33] J. Hillier, K. Ono, K. Ibukuro, F. Liu, Z. Li, M. H. Khaled, H. N. Rutt, I. Tomita, Y. Tsuchiya, K. Ishibashi, and S. Saito, *Nanotechnology* **32**, 260001 (2021).
- [34] M. S. Tyagi and R. Van Overstraeten, *Solid-State Electron.* **26**, 577 (1983).
- [35] L. F. Mattheiss and J. R. Patel, *Phys. Rev. B* **23**, 5384 (1981).
- [36] J. C. Slater and G. F. Koster, *Phys. Rev.* **94**, 1498 (1954).
- [37] S. Datta, A. Das, and S. Yarlagadda, *Phys. Rev. B* **71**, 235118 (2005).
- [38] J. Bonča and S. A. Trugman, *Phys. Rev. B* **64**, 094507 (2001).
- [39] B. E. Kane, *Nature (London)* **393**, 133 (1998).
- [40] P. Willke, Y. Bae, K. Yang, J. L. Lado, A. Ferrón, T. Choi, A. Ardavan, J. Fernández-Rossier, A. J. Heinrich, and C. P. Lutz, *Science* **362**, 336 (2018).